scientific reports

OPEN

Severe level of photochemical oxidants (O_x) over the western coast of Japan during autumn after typhoon passing

Syuichi Itahashi

Photochemical oxidants (O_x; mainly O_3) are a concern in East Asia. Because of the prevailing westerly wind in the midlatitudes, O_3 concentration generally shows a high in spring over Kyushu Island, western Japan, and O_x warnings have been issued in spring. However, the record from 2000 to 2021 of O_x warning days in Kyushu Island contains one warning case in autumn 2020. Interestingly, a typhoon had passed the day before this O_x warning. To relate these events, a modelling simulation was conducted and it showed the transboundary O_3 transport from the Asian continent to the western coast of Japan due to the strong wind field determined by the location of Typhoon Haishen (2020). The sensitivity simulations for changing Chinese anthropogenic sources suggested that both nitrogen oxides (NO_x) and volatile organic compound (VOC) emission regulations in China could decrease high O_3 over the downwind region of Japan. Furthermore, VOC emission regulation in China led to an overall O_3 decrease in East Asia, whereas NO_x emission regulation in China had complex effects of decreasing (increasing) O_3 during the daytime (nighttime) over China. The association between air quality and meteorology related to typhoons should be considered along with global warming in the future.

Photochemical oxidants (O_x), which mainly consist of tropospheric ozone (O_3), are related to chemical reactions involving nitrogen oxides (NO_x) and volatile organic compounds (VOCs)[1]. O_x causes urban smog, poses major risks to human health and the natural environment, and is an important greenhouse gas[2]. The Japanese environmental quality standard (EQS) for O_x was established in 1973, and hourly O_x values should not exceed 0.06 ppm (118 μg/m³)[3]. In addition, the Air Pollution Control Law (Paragraph 1, Article 23) stipulates that when hourly O_x concentration exceeds 0.12 ppm and the status is expected to continue due to weather conditions, a warning should be issued to prevent damage to human health or the living environment. The EQS has not been satisfied at most monitoring stations in Japan, and this is a continuing issue that should be solved[4,5]. In general, high O_x concentrations and subsequent O_x warnings have generally occurred in spring over western Japan and in summer toward eastern Japan (e.g., Osaka, Nagoya, and Tokyo). This seasonal variation of O_x in Japan is related to the transboundary O_x transport from the Asian continent during spring and local photochemical production in Japan during summer[6–11]. A recent report on Japanese local photochemical production found a decreasing trend in the 3-year average of the annual 99th percentile of the daily maximum 8-h concentration (a new index for evaluating O_x), especially over the Kanto region (e.g., Tokyo)[12], and this result suggested that transboundary O_x pollution has an important effect over Japan. The worsening of O_x pollution in East Asia has been a concern recently[13–15]; thus, the effect of transboundary transport on O_x behaviour is the focus of the present work.

Over Kyushu Island, western Japan, high O_x concentrations and related warnings are generally issued during spring. The summary of the number of O_x warning days from 2000 to 2021 over Kyushu Island is presented in Fig. 1. The O_x warning days have mostly been observed in May, and sometimes in April and June. In Nagasaki Prefecture, located on western Kyushu Island, an O_x warning was issued for the first time in May 2006. However, there was one warning day in September 2020 in Nagasaki Prefecture (Fig. 1). This warning was issued on Goto Island (westernmost Nagasaki Prefecture, Fig. 1) on 8 September, 2020 at 15:00 local time when an O_x concentration of 123 ppb was observed, the maximum concentration was recorded as 126 ppb at 16:00 local time, and the warning was canceled at 19:00 local time. In the present study, this severe O_x concentration event was analysed because this is the first case of a warning issued in autumn in Nagasaki Prefecture.

Sustainable System Research Laboratory (SSRL), Central Research Institute of Electric Power Industry (CRIEPI), Abiko, Chiba 270-1194, Japan. email: isyuichi@criepi.denken.or.jp
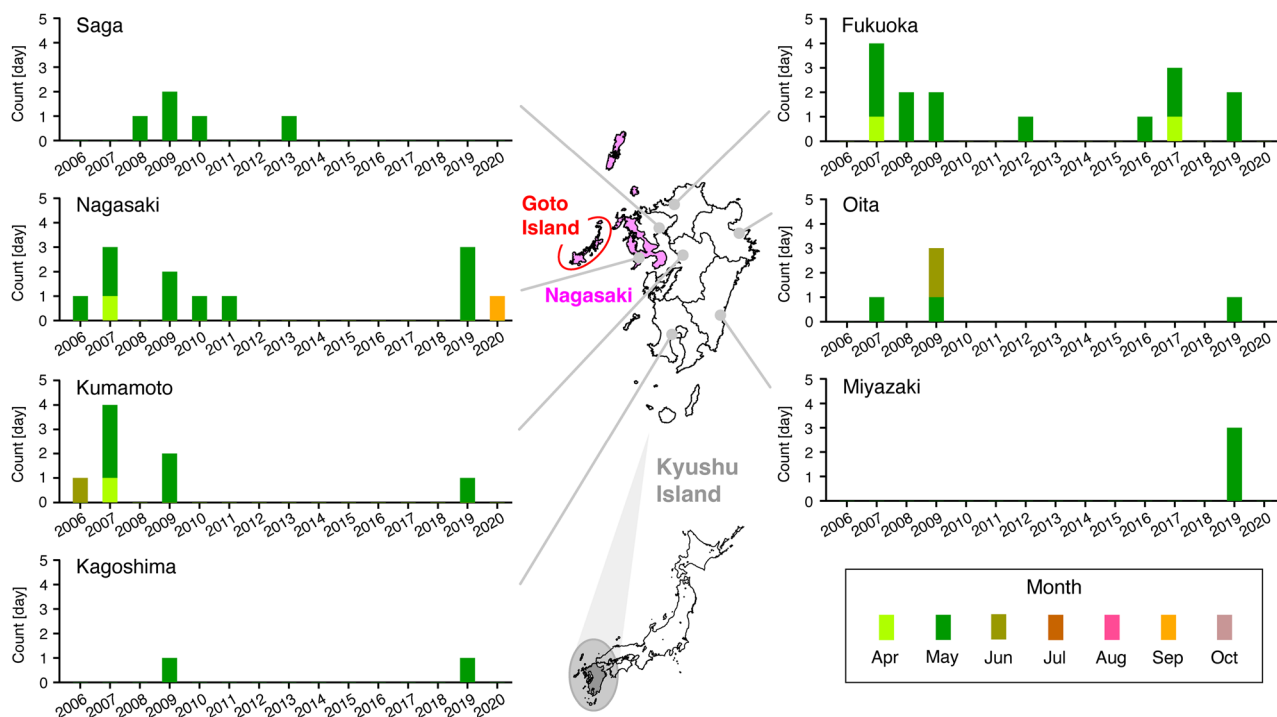
Figure 1. Record of the O_x warning days for severe concentrations (see, text for this definition) from 2000 to 2021 over seven prefectures on Kyushu Island, Japan. The colours indicate the month. At the start of this study, the confirmed values of AEROS were reported up to 2021[12], and no days were reported in 2000–2005 and 2021 over all prefectures in Kyushu Island. The maps were generated with GMT (https://docs.generic-mapping-tools.org/dev/index.html).

Results

First, the meteorological conditions in September 2020 were analysed. Typhoons Maysak (2020) and Haishen (2020) occurred in this period[16]. Typhoon Maysak (2020) formed on 27 August, 2020 over the eastern Philippines and passed over western Kyushu Island on 2–3 September, and Typhoon Haishen (2020) formed on 31 August, 2020 over the Northwest Pacific and passed over western Kyushu Island on 6–7 September (Supplementary Fig. S1). The O_x warning on Goto Island in September 2020 was issued the day after Typhoon Haishen (2020) passed. Typhoons are usually associated with hazards, such as strong winds, storm surges, and rainfall, that can cause considerable damage and disruption. Although such a strong wind field could simply result in good ventilation and reduce air pollutant concentrations, several studies have reported that typhoons degraded air quality in terms of $PM_{2.5}$[17,18], O_x[19,20], and deposition[21,22]. Because the O_x warning issued in September 2020 occurred in a remote area of Goto Island, westernmost Nagasaki Prefecture, the horizontal distribution over East Asia should also be examined. Thus, a numerical modelling simulation covering the whole of East Asia (Supplementary Fig. S2) was applied to analyse this severe O_x event further (see "Methods" section for details of the modelling).

The surface pressure anomaly, which is a unique characteristic of typhoons, was investigated and evaluated with the typhoon best-track data[16]. The typhoon tracks (Supplementary Fig. S1) and the simulated surface pressure anomaly are shown in Fig. 2. In this comparison, the anomaly was calculated by the difference between the surface pressure during each typhoon and the 1-month average (from 15 August, 2020 to 14 September, 2020; see "Methods" section). The typhoon best-track data and the simulated lower anomaly associated with Typhoons Maysak (2020) and Haishen (2020) agreed well. The comparison shown in Fig. 2 indicated that the general features of typhoon movement were captured well in the present modelling simulations.

The meteorological parameters were measured by the Automated Meteorological Data Acquisition System (AMeDAS) at the Fukue observatory, which is on Goto Island (Fig. 1), and the corresponding simulated results are shown in Fig. 3. The pressure (Fig. 3a) was simulated well, and the decrease in pressure was larger in the period when Typhoon Haishen (2020) passed compared with that when Typhoon Maysak (2020) passed. The precipitation (Fig. 3b) was generally underestimated but the timing was well captured. The wind speed (Fig. 3c) and direction (Fig. 3d) were also well captured, although the wind speed tended to be overestimated. This overestimation was mainly due to the insufficient wind reduction over the land. In addition to the case at Fukue in Fig. 3, another validation at Nomozaki, southern Nagasaki Prefecture is presented in Supplementary Fig. S3. The Nomozaki site observed a record-breaking maximum instantaneous wind velocity (59.4 m/s, the corresponding wind velocity in 1 h was 43.7 m/s) during Typhoon Haishen (2020), and such wind speeds were generally captured by the modelling system. These evaluations of the meteorological parameters showed that the present modelling system reproduced the meteorological field well, especially the features when the typhoons passed.
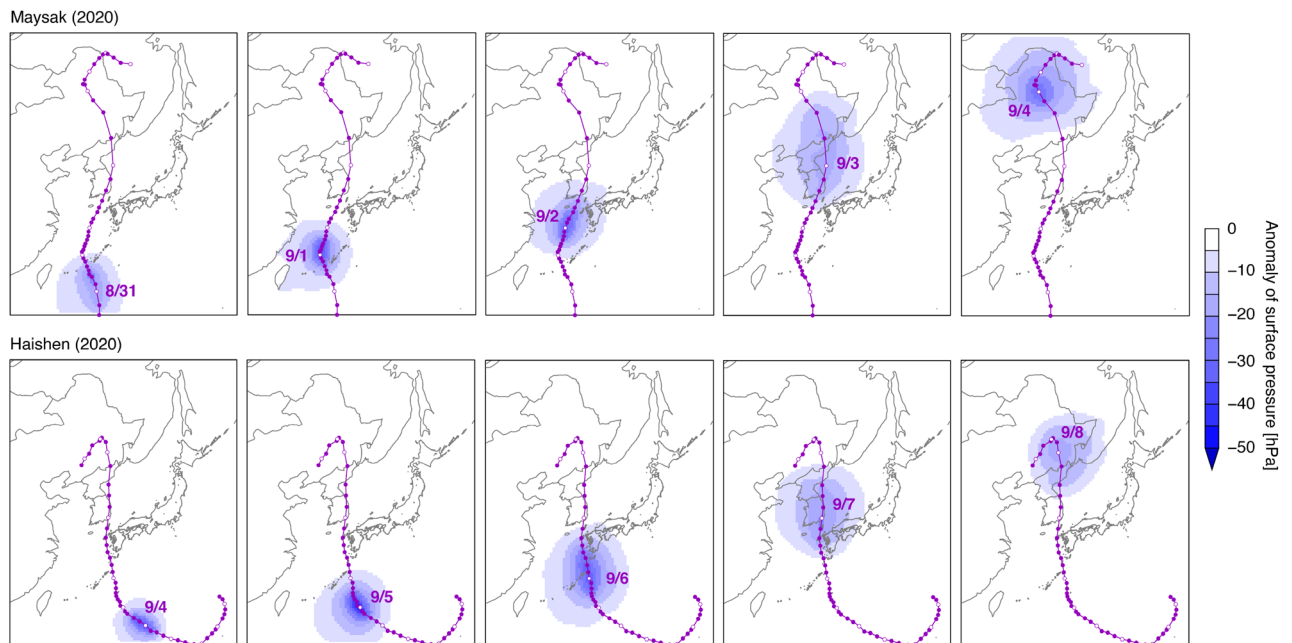
Figure 2. Best-track data of (top) Typhoon Maysak (2020) and (bottom) Typhoon Haishen (2020) with surface pressure anomalies simulated by the WRF meteorological model. The maps were generated with GMT (https://docs.generic-mapping-tools.org/dev/index.html).
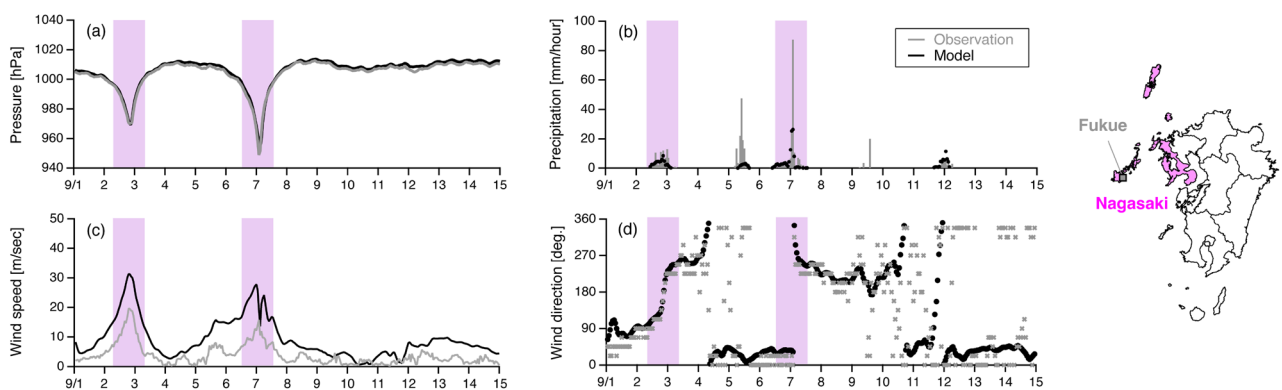

Figure 3. Comparison of meteorological fields of (**a**) pressure, (**b**) precipitation, (**c**) wind speed, and (**d**) wind direction from observations (grey) and the model (black) at Fukue, AMeDAS station in Nagasaki Prefecture. The purple shading indicates the days affected by Typhoon Maysak (2020) and Typhoon Haishen (2020). The maps were generated with GMT (https://docs.generic-mapping-tools.org/dev/index.html).

The modelling performance for O_3 concentration in Nagasaki Prefecture is shown in Fig. 4. The O_3 concentration was lower during two typhoon periods (purple shading, see also Fig. 3). After Typhoon Maysak (2020) passed on 3 September, 2020, the O_3 concentration was slightly increased to 60–80 ppbv at all sites in Nagasaki Prefecture. Subsequently, due to Typhoon Haishen (2020) passing, O_3 concentration was decreased to 20 ppbv on 7 September, 2020. There was a sharp increase in O_3 concentration after Typhoon Haishen (2020) passed, and the O_3 concentration reached its peak from 8 to 9 September, 2020. This maximum concentration was close to 100 ppbv in cities in the main parts of Nagasaki Prefecture, whereas on the remote islands of Nagasaki Prefecture (Tsushima, Iki, and Goto) it was close to 120 ppbv, which is the alert level for severe O_3 pollution. Of these three remote sites, only Goto Island issued an O_x alert, and the present modelling system captured this high O_3 concentration exceeding 120 ppbv well. The statistical metrics scores (see the "Methods" section for their definitions) are also shown in Fig. 4. The correlation coefficient (*R*) was from 0.61 to 0.91, the normalized mean bias (*NMB*) was from + 5.8% to + 31.2%, and the normalized mean error (*NME*) was from + 15.9% to 31.2%. Except for the grid corresponding to Nagasaki city (#3 in Fig. 4), these metrics met the model performance criteria. These evaluations of O_3 concentration also demonstrated that the present modelling system reproduced O_3 pollution in Nagasaki Prefecture. In addition to these validations in Nagasaki prefecture, the vertical O_3 profiles are compared in Supplementary Fig. S4 and show that O_3 concentration from the surface to the middle stratosphere (approximately 20 km) was also captured well by the modelling system. The NO_2 column density observed by
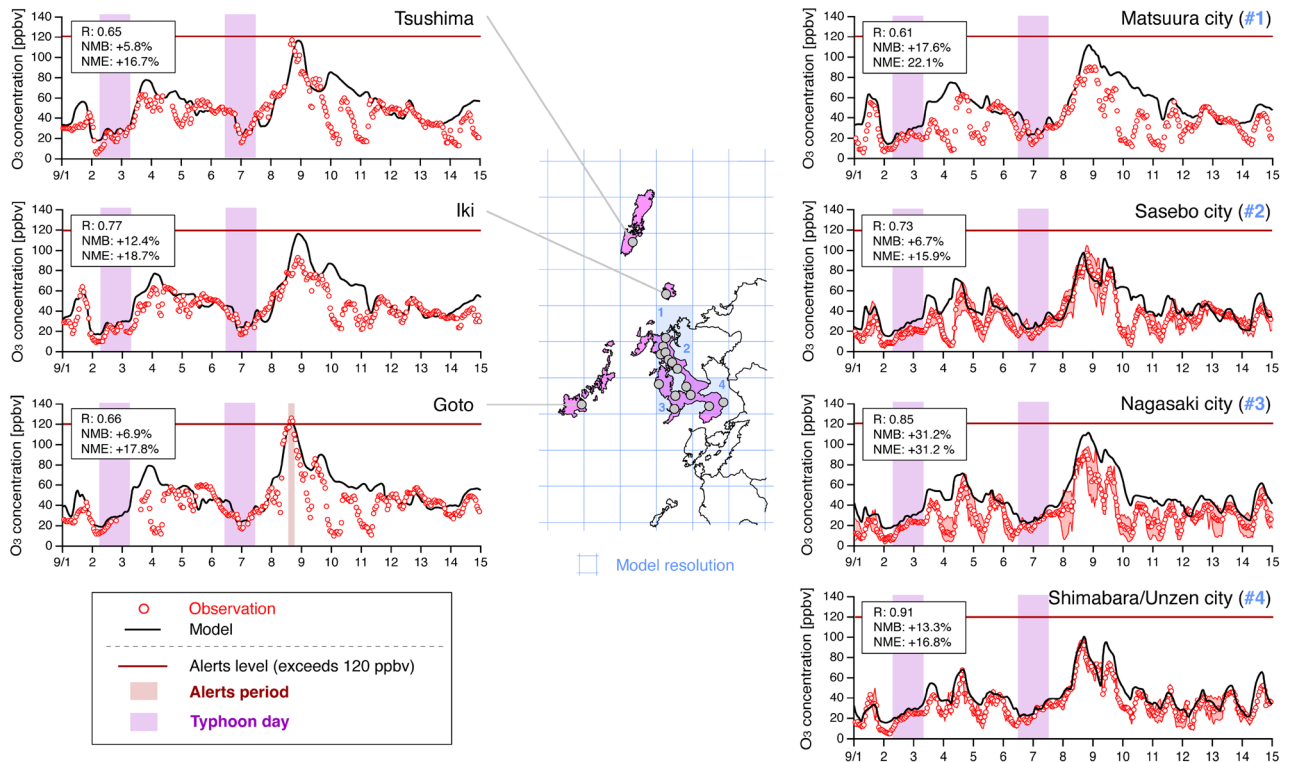
Figure 4. Comparison of O_3 concentrations from observations (red) and the model (black) at all 17 sites in Nagasaki Prefecture. The purple shading indicates the days affected by typhoons (Fig. 3). The dark-red shading indicates the period of O_x alerts. When the measurement sites were allocated in the same model grid, the averaged values were used to evaluate the model, and the minimum and maximum concentrations are indicated by red shading. The statistical scores are shown in the box. The maps were generated with GMT (https://docs.generic-mapping-tools.org/dev/index.html).

the satellite is compared in Supplementary Fig. S5 and a high NO_2 concentration in the eastern part of China was generally captured. Based on these results, we confirmed the modelling system in this study captured the meteorological field and O_3 concentration in early September 2020. The reasons for the O_x alert event over Goto Island despite the typhoon passing are discussed.

Discussion

To identify the reasons for the high O_3 concentration that triggered the alert, the horizontal distribution pattern from 7 to 9 September, 2020 is shown in Fig. 5. At midnight on 7 September (Fig. 5a), high O_3 concentration (70–90 ppbv; yellow to orange, which exceeds the Japanese EQS) was seen over the East Asian ocean adjacent to the Asian continent. In addition, the typhoon was over Goto Island, and westerly or north-westerly wind fields prevailed over the East China Sea. At this time, the O_3 concentrations over Goto Island and other sites in Nagasaki Prefecture were low (20 ppbv; light green, see also Fig. 4). The high O_3 concentrations stretched into the East China Sea (Fig. 5b), and O_3 was produced during the daytime and the concentration increased on 7 September (Fig. 5c). During the night of 7 September (Fig. 5d), the high O_3 concentration over mainland China was decreased to a low concentration by NO titration and deposition, whereas the high O_3 concentration (120 ppbv; dark red, alert level) remained over the East China Sea. During this time, Typhoon Haishen (2020) was over the northern part of the Korean peninsula, and southerly and south-westerly wind fields transported this high O_3 concentration to Kyushu Island (Fig. 5e and f). During the daytime on 8 September (Fig. 5g), this air mass with O_3 higher than 120 ppbv reached Goto Island on the western edge of Kyushu Island; hence, the O_x alert was issued. Then, the air mass was transported to the Tsushima Strait (between Kyushu Island and the Republic of Korea) due to the south-westerly wind affected by Typhoon Haishen (2020) in Liaoning Province, northeastern China (Fig. 5h and i). This analysis of the simulated O_3 spatial distribution suggested transboundary O_3 transport from the Asian continent to the western part of Japan, and the wind system caused by Typhoon Haishen (2020) was important in determining the air mass transport. Based on the analysis at the top of the boundary layer (approximately 750 hPa) shown in Supplementary Fig. S5, this high transboundary O_3 transport was limited near the surface level.

The transboundary O_3 transport after the typhoon passing was clarified, and mitigation of this severe pollution is a concern. Finally, the effects of emission regulations are discussed based on the sensitivity simulations. The changes in O_3 concentration when 20% reductions in Chinese VOC and NO_x emissions (ΔC_V in Eq. (4) and ΔC_N in Eq. (5), see "Methods" section) were applied are shown in Figs. 6 and 7, respectively, and those for simultaneous VOC and NO_x emission reductions are shown in Supplementary Fig. S6. The reduction in
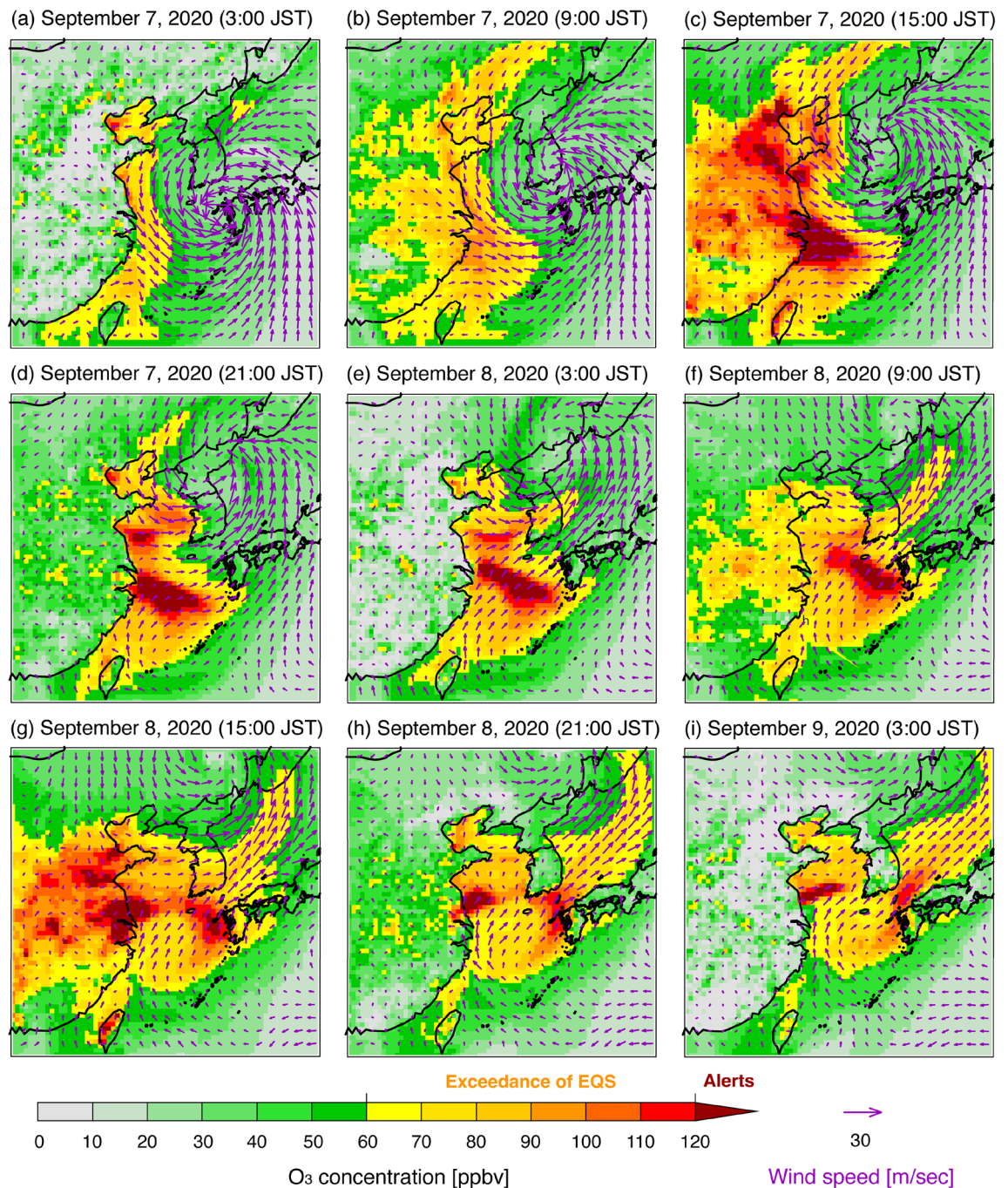
Figure 5. Simulated spatial distributions of O_3 concentration at the surface level over East Asia before, during, and after the O_x alert on Goto Island, Nagasaki Prefecture. The maps were generated with gtool3 (http://www. gfd-dennou.org/library/gtool/index.htm.en).

anthropogenic Chinese VOC emissions always helped to reduce O_3 concentration during the analysis period (Fig. 6). In contrast, the reduction in anthropogenic Chinese NO_x emissions had complex effects because it caused both O_3 decreases and increases (Fig. 7). The increase in O_3 was observed only over mainland China from night to early morning and was associated with the weakening NO titration effect due to the NO_x emission reduction. During the daytime, Chinese NO_x emission reduction led to an O_3 decrease, and moreover, it always led to an O_3 decrease over the downwind region of Japan and this impact was greater than Chinese VOC emission regulation. Therefore, NO_x emission regulations in China should consider these negative aspects. Recently, the aggravating effect of NO_x emission regulations on O_3 pollution has been reported in China[23,24], and the present results are also consistent with these findings.

Due to global warming, the frequency of typhoons will decrease, whereas their intensity will increase[25,26]. Similar future changes are also reported for the western North Pacific, and will lead to destructive threats by
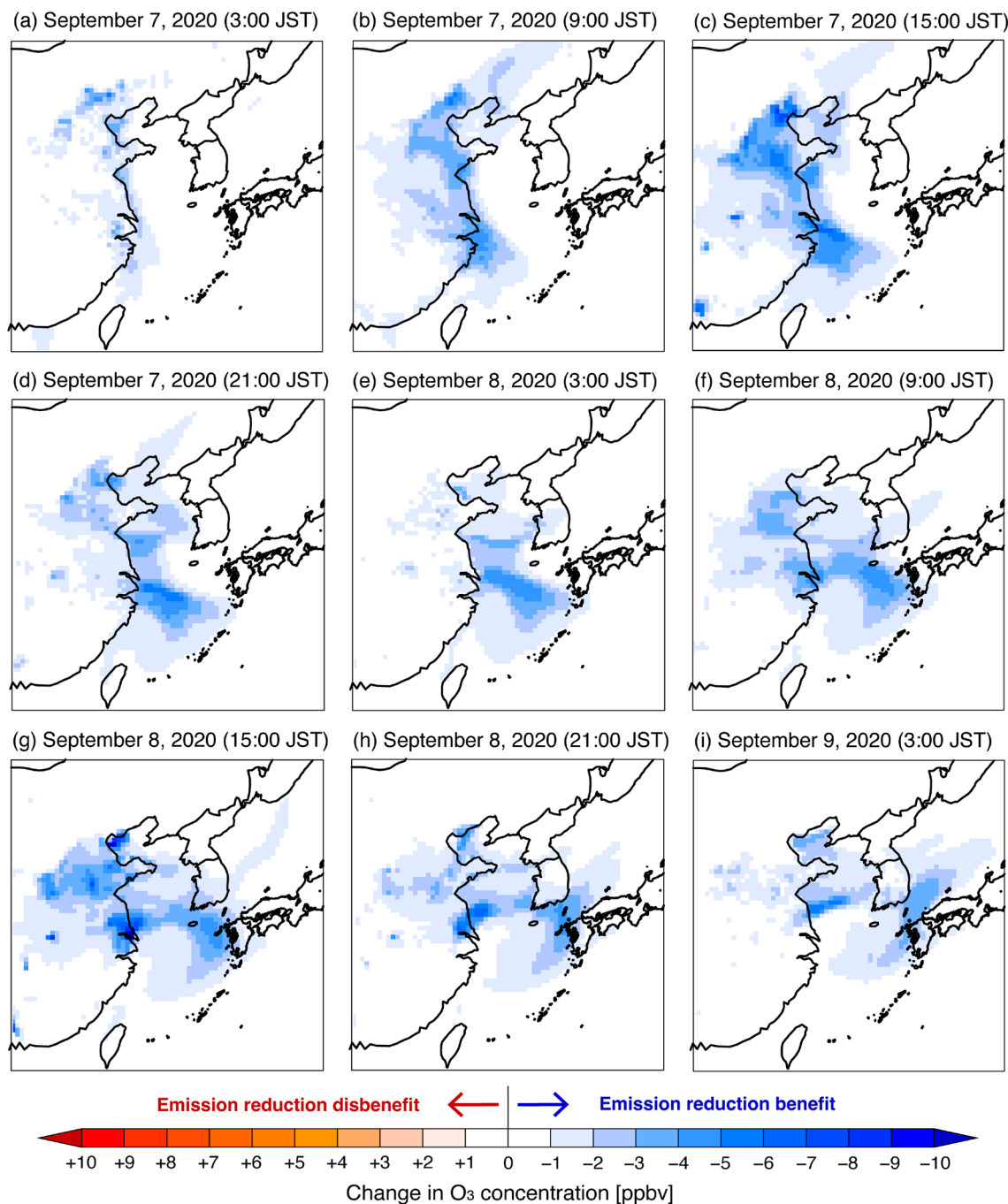
Figure 6. Simulated spatial distributions of change in O_3 concentration with anthropogenic VOC emissions in China decreased by 20% (ΔC_V in Eq. (4)). Red indicates increased O_3 concentration in the sensitivity simulation (i.e., emission reduction disbenefit), whereas blue indicates decreased O_3 concentration (i.e., emission reduction benefit). The maps were generated with gtool3 (http://www.gfd-dennou.org/library/gtool/index.htm.en).

stronger wind fields and intense precipitation[27,28]. As shown in the present study, high levels of O_x over East Asia could be related to the meteorological fields associated with typhoons. Although precursor emission reduction could mitigate both global warming and air quality[29], the behaviour of air pollutants related to the meteorological field should be continuously paid attention in future studies.

Methods
Observations
Ground-based observation of air pollutants that are regulated by EQS (carbon monoxide (CO), sulfur dioxide (SO_2), nitrogen dioxide (NO_2), O_x, suspended particulate matter (SPM), and particulate matter with an aerodynamic diameter less than 2.5 μm ($PM_{2.5}$)) are routinely measured by the Atmospheric Environmental Regional Observation System (AEROS) (https://soramame.env.go.jp). AEROS is divided into monitoring of ambient air
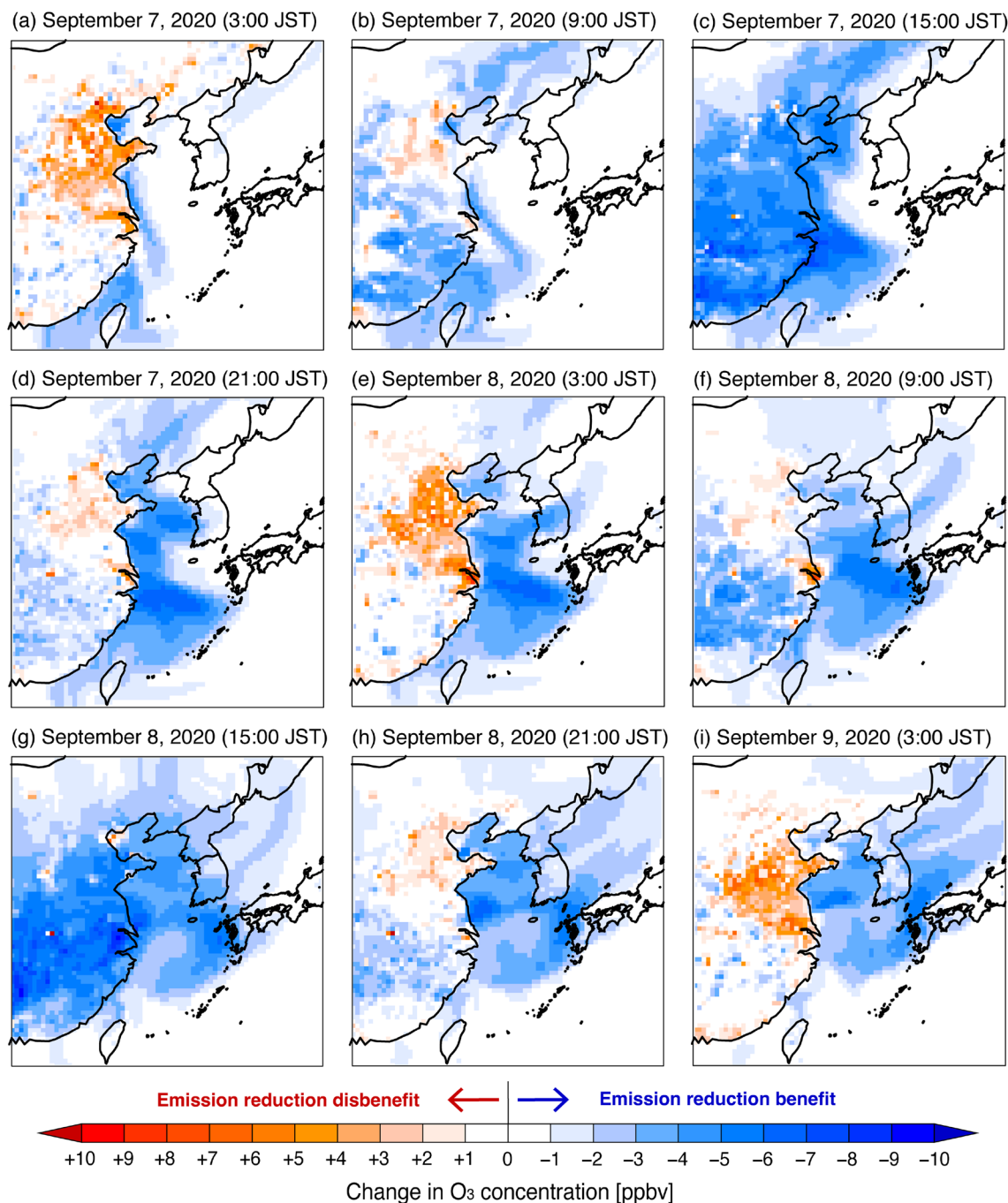
Figure 7. Simulated spatial distributions of change in O_3 concentration with anthropogenic NO_x emissions in China decreased by 20% (ΔC_N in Eq. (5)). Red color indicates increased O_3 concentration in the sensitivity simulation (i.e., emission reduction disbenefit), whereas blue color indicates decreased O_3 concentration (i.e., emission reduction benefit). The maps were generated with gtool3 (http://www.gfd-dennou.org/library/gtool/index.htm.en).

quality by ambient air pollution monitoring stations (APMSs) and of air pollution, particularly from automobiles, by roadside air pollution monitoring stations (RAPMSs). In this study, APMSs data was used in Nagasaki Prefecture. The O_x measurements were obtained by the neutral-buffered potassium iodide method or ultraviolet absorption spectrometry. Although ultraviolet absorption spectrometry only detects O_3, it was approved in 1996 as the standard method for measuring O_x concentrations. For the consistency of the measurement dataset, O_x concentrations based on the ultraviolet absorption spectrometry at APMSs were used in this study. Nagasaki Prefecture, which is the focus of this study, is on the western coast of Japan (Fig. 1). Previous studies have clarified transboundary air pollution using measurement data here because of its location, especially at remote island sites (e.g., Goto Island) where domestic emissions are small[30–32]. There are 17 sites in total in Nagasaki Prefecture, and

the model grids numbered 1 to 4 (Fig. 4) include 1, 6, 5, and 2 APMSs measurements sites in the same model grid, respectively, and the averaged O_x concentration in the same model grid was compared with the simulation result.

In addition to the ground-based observation in Nagasaki Prefecture, vertical O_3 profiles measured by ozone-sonde distributed from the World Ozone and Ultraviolet Radiation Data Centre (WOUDC) (https://woudc.org/data/explore.php?dataset=ozonesonde) were used. During the first part of September 2020, the available ozone-sonde data in East Asia were from 2 and 9 September, 2020 at King's Park, Hong Kong (22.31° N, 114.17° E) and 3 and 8 September, 2020 at Pohang, the Republic of Korea (36.03° N, 129.38° E). A total of four vertical profile data were compared with the model result. In terms of the precursor of O_3, satellite-derived tropospheric NO_2 column densities can be a proxy of NO_x emissions[33]. The level 2 of swath measurement data taken by Ozone Monitoring Instrument (OMI) onboard the Aura was used[34], and the information of the averaging kernel was applied for model output for fair comparison.

Modelling simulation

To understand the horizontal distribution pattern of O_x, the modelling simulation was conducted using the regional chemical transport model of the Community Multiscale Air Quality (CMAQ) version 5.3.3[35]. The simulation domain covering East Asia was configured by 215×120 grid points with a horizontal resolution of 36 km (Supplementary Fig. S2), and 44 non-uniformly spaced layers from the surface to 50 hPa with a vertical resolution of approximately 20 m for the surface layer[36]. The meteorological fields for driving CMAQ were prepared by the Weather Research and Forecasting (WRF) model version 4.4[37]. Modelling simulations were started from 8 August, 2020 and analysed from 15 August, 2020 to 14 September, 2020, discarding the first week as a spin-up period. SAPRC07tic[38] and aero7[39] were used for gas-phase and aerosol chemistry, respectively, and the NO_2 aqueous-phase reaction in the SO_4^{2-} oxidation process[40] and better consideration of trace metal ion-catalysed O_2 oxidation[41] were included based on previous studies. The initial and lateral boundary conditions were prepared from autumn-averaged values of the extended CMAQ over the northern hemisphere (H-CMAQ)[42].

The emissions inventories were prepared as follows. Anthropogenic emissions except those in China were based on Hemispheric Transport of Air Pollution (HTAP) version 3[43]. The latest available year is 2018 and this dataset with monthly variation is used. For China, the emission projections were based on the Multi-resolution Emission Inventory in China (MEIC), which includes the variation of Chinese emissions during the COVID-19 pandemic[43]. From this estimation, the anthropogenic emissions had almost recovered in August–September to the levels before the COVID-19 period, consistent with the author's previous investigation into the transboundary $PM_{2.5}$ transport[31]. Because the ship SO_2 emissions were regulated according to the International Convention for the Prevention of Pollution from Ships (MARPOL) from 1 January, 2020, a reduction in SO_2 emissions of 77% was applied based on a report by the International Maritime Organization (IMO)[45]. Biogenic emissions were prepared from the Model of Emissions of Gases and Aerosols from Nature (MEGAN)[46] using the WRF-simulated meteorological field, and biomass-burning emissions were taken from the Global Fire Emissions Database (GFED) version 4.1[47]. SO_2 emissions from 17 volcanoes in Japan were prepared from a measurement report by the Japan Meteorological Agency[48].

The model performance was evaluated statistically using metrics R, NMB, and NME, defined as

$$R = \frac{\sum_1^N \left(O_i - \overline{O}\right)\left(M_i - \overline{M}\right)}{\sqrt{\sum_1^N \left(O_i - \overline{O}\right)^2}\sqrt{\sum_1^N \left(M_i - \overline{M}\right)^2}}, \tag{1}$$

$$NMB = \frac{\sum_1^N \left(M_i - O_i\right)}{\sum_1^N O_i}, \tag{2}$$

$$NME = \frac{\sum_1^N |M_i - O_i|}{\sum_1^N O_i}, \tag{3}$$

where N is the total number of paired observations (O) and models (M), and the corresponding averages are $\overline{O}$ and $\overline{M}$, respectively. The recommended metrics for 1-h O_3 based on a literature review for the United States[49] reported as the model performance goals are $R > 0.75$, $NMB < \pm 5\%$, and $NME < +15\%$, and the model performance criteria are $R > 0.50$, $NMB < \pm 15\%$, and $NME < +25\%$ with no cutoff for R and a 40 ppbv cutoff for NMB and NME.

To estimate the change in O_3 production from the VOC and NO_x precursors, sensitivity simulations that perturbed anthropogenic VOC emissions, anthropogenic NO_x emissions, and simultaneous anthropogenic VOC and NO_x emissions in China were performed in addition to the base-case simulation, which includes all emission sources. The perturbation range was a 20% emission reduction from the base-case, which is typical for potential emission controls[8]. The change in O_3 concentration from the base-case simulation was calculated based on the following three definitions. In this study, the changes in concentration were directly shown and not scaled to be expressed as sensitivities.

$$\Delta C_V = C_{\text{Chinese VOC emission 20\% reduction case}} - C_{\text{Base-Case}}, \tag{4}$$

$$\Delta C_N = C_{\text{Chinese NOx emission 20\% reduction case}} - C_{\text{Base-Case}}, \tag{5}$$

$$\Delta C_{NV} = C_{\text{Chinese VOC and NOx emission 20\% reduction case}} - C_{\text{Base-Case}}, \qquad (6)$$

Data availability

The datasets generated during and/or analysed during the current study are available from the corresponding author on reasonable request.

References

1. Seinfeld, J. H. & Pandis, S. N. *Atmospheric Chemistry and Physics—From Air Pollution to Climate Change* 3rd edn. (Wiley, Uk, 2016).
2. Jacobson, M. Z. *Air Pollution and Global Warming* 2nd edn. (Cambridge University Press, 2012).
3. Ministry of the Environment. Environmental quality standads in Japan—Air quality. https://www.env.go.jp/en/air/aq/aq.html (2022).
4. Wakamatsu, S., Morikawa, T. & Ito, A. Air pollution trends in Japan between 1970 and 2012 and impact of urban air pollution countermeasures. *Asian J. Atmos. Environ.* **7**, 177–190 (2013).
5. Ito, A., Wakamatsu, S., Morikawa, T. & Kobayashi, S. 30 years of air quality trends in Japan. *Atmosphere* **12**, 1072 (2021).
6. Itahashi, S., Uno, I. & Kim, S.-T. Seasonal source contributions of tropospheric ozone over East Asia based on CMAQ-HDDM. *Atmos. Environ.* **70**, 204–217 (2013).
7. Itahashi, S., Hayami, H. & Uno, I. Comprehensive study of emission source contributions for tropospheric ozone formation over East Asia. *J. Geophys. Res. Atmos.* **120**, 331–358. https://doi.org/10.1002/2014JD022117 (2015).
8. Chatani, S., Shimadera, H., Itahashi, S. & Yamaji, K. Comprehensive analyses of source sensitivities and apportionments of $PM_{2.5}$ and ozone over Japan via multiple numerical techniques. *Atmos. Chem. Phys.* **20**, 10311–10329 (2020).
9. Chatani, S. *et al.* Identifying key factors influencing model performance on ground-level ozone over urban areas in Japan through model inter-compasirons. *Atmos. Environ.* **223**, 117255 (2020).
10. Itahashi, S., Mathur, R., Hogrefe, C., Napelenok, S. L. & Zhang, Y. Modeling stratospheric intrusion and trans-Pacific transport on tropospheric ozone using hemispheric CMAQ during April 2010–Part 2: Examination of emission impacts based on the higher-order decoupled direct method. *Atmos. Chem. Phys.* **20**, 3397–3413 (2020).
11. Chatani, S. *et al.* Effectiveness of emission controls implemented since 2000 on ambient ozone concentrations in multiple timescales in Japan: An emission inventory development and simulation study. *Sci. Tot. Env.* **894**, 165058 (2023).
12. Ministrry of the Environment. Air Pollution Status in Fiscal Year 2021. Webpage in Japanese. https://www.env.go.jp/press/press_01411.html (2023).
13. Li, J. *et al.* MICS-Asia III: Overview of model intercomparison and evaluation of acid deposition over Asia. *Atmos. Chem. Phys.* **20**, 2667–2693 (2020).
14. Wang, Y. *et al.* Contrasting trends of $PM_{2.5}$ and surface-ozone concentrations in China from 2013 to 2017. *Natl. Sci. Rev.* **7**, 1331–1339 (2020).
15. Wang, T. *et al.* Ground-level ozone pollution in China: A synthesis of recent findings on influencing factors and impacts. *Environ. Res. Lett.* **17**, 063003 (2022).
16. Japan Meteorological Agency. Regional Specialized Meteorological Center (RSMC) Tokyo—Typhoon Center. https://www.jma.go.jp/jma/jma-eng/jma-center/rsmc-hp-pub-eg/RSMC_HP.htm (2023).
17. You, S., Kang, Y.-H., Kim, B.-U., Kim, H. C. & Kim, S. The role of a distant typhoon in extending a high $PM_{2.5}$ episode over North-east Asia. *Atmos. Environ.* **257**, 118480 (2021).
18. Lin, C.-Y. *et al.* Air quality deteriotation episode associated with a typhoon over the complex topography environment in central Taiwan. *Atmos. Chem. Phys.* **21**, 16893–16910 (2021).
19. Ouyang, S. *et al.* Impact of a subtropical high and a typhoon on a severe ozone pollution episide in the Pearl River Delta, China. *Atmos. Chem. Phys.* **22**, 10751–10767 (2022).
20. Wang, N. *et al.* Typhoon-boosted biogenic emission aggravates cross-regional ozone pollution in China. *Sci. Adv.* **8**, eabl6166 (2022).
21. Tan, Q. *et al.* Unexpected high contribution of in-cloud wet scavenging to nitrogen deposition induced by pumping effect of typhoon landfall in China. *Environ. Res. Comm.* **5**, 021005 (2023).
22. Zhang, Y. *et al.* Enhanced wet deposition of nitrogen induced by a landfalling typhoon over East Asia: Implications for the marine eco-environment. *Environ. Sci. Tech. Lett.* **9**, 1014–1021 (2023).
23. Wang, N. *et al.* Aggravating O_3 pollution due to NO_x emission control in eastern, China. *Sci. Total Environ.* **677**, 732–744 (2019).
24. Chen, X. *et al.* Chinese regulations are working—why is surface ozone over industrialized areas still high? Applying lessons from northeast US air quality evolution. *Geophys. Res. Lett.* **48**, e2021GL092816 (2021).
25. Knutson, T. *et al.* Tropical cyclones and climate change assessment. Part I: Detection and attribution. *Bull. Am. Meteorol. Soc.* **100**, 1987–2007 (2019).
26. Knutson, T. *et al.* Tropical cyclones and climate change assessment. Part II: Projected response to anthropogenic warming. *Bull. Am. Meteorol. Soc.* **101**, 303–322 (2020).
27. Yoshida, K. *et al.* Future changes in tropical cyclone activity in high-resolution large-ensemble simulations. *Geophys. Res. Lett.* **44**, 9910–9917 (2017).
28. Hsu, P.-C. *et al.* Future changes in the frequency and destructiveness of lanfalling tropical cyclones over East Asia projected by high-resolution AGCMs. *Earths Future* **9**, e2020EF001888 (2021).
29. Nakajima, T. *et al.* A development of reduction scenarios of the short-lived climate pollutants (SLCPs) for mitigating global warming and environmental problems. *Prog. Earth Planet. Sci.* **7**, 33 (2020).
30. Uno, I. *et al.* Paradigm shift in aerosol chemical composition over regions downwind of China. *Sci. Rep.* **10**, 21748. https://doi.org/10.1038/s41598-020-63592-6 (2020).
31. Itahashi, I., Yamamura, Y., Wang, Z. & Uno, I. Returning long-range $PM_{2.5}$ transport into the leeward of East Asia in 2021 after Chinese economic recovery from the COVID-19 pandemic. *Sci. Rep.* **12**, 5539. https://doi.org/10.1038/s41598-022-09388-2 (2022).
32. Kanaya, I. *et al.* Rapid reduction in black carbon emissions from China: Evidence from 2009–2019 observations on Fukue Island, Japan. *Atmos. Chem. Phys.* **20**, 6339–6356 (2020).
33. Itahashi, S. *et al.* Inverse estimation of NO_x emissions over China and India 2005–2016: Contrasting recent trends and future perspectives. *Environ. Res. Lett.* **14**, 124020 (2019).
34. Nickolay, A. *et al.* OMI/Aura nitrogen dioxide (NO_2) total and tropospheric column 1-orbit L2 Swath 13x24 km V003, Greenbelt, MD, USA, Goddard Earth Sciences Data and Information Services Center (GES DISC). 10.5067/Aura/OMI/DATA2017 (2019).
35. U.S. Environmental Protection Agency. CMAQ (Version 5.3.3). 10.5281/zenodo.5213949 (2021).

36. Itahashi, S., Mathur, R., Hogrefe, C. & Zhang, Y. Modeling stratospheric intrusion and trans-Pacific transport on tropospheric ozone using hemispheric CMAQ during April 2010–Part 1: Model evaluation and air mass characterization for stratosphere–troposphere transport. *Atmos. Chem. Phys.* **20**, 3373–3396 (2021).
37. Skamarock, W. C. *et al. A Description of the Advanced Research WRF Version 4. NCAR Tech. Note, NCAR/TN-556+STR.* 162 (National Center for Atmospheric Research, 2019).
38. Xie, Y. *et al.* Understanding the impact of recent advances in isoprene photooxidation on simulations of regional air quality. *Atmos. Chem. Phys.* **13**, 8439–8455 (2013).
39. Xu, L. *et al.* Experimental and model estimates of the contributions from biogenic monoterpenes and sesquiterpenes to secondary organic aerosol in the southeastern United States. *Atmos. Chem. Phys.* **18**, 12613–12637 (2018).
40. Itahashi, S., Uchida, R., Yamaji, K. & Chatani, S. Year-round modeling of sulfate aerosol over Asia through updates of aqueous-phase oxidation and gas-phase reactions with stabilized Criegee intermediates. *Atmos. Environ. X.* **12**, 100123 (2021).
41. Itahashi, S. *et al.* Role of dust and iron solubility in sulfate formation during the long-range transport in East Asia evidenced by ^{17}O-excess signatures. *Environ. Sci. Technol.* **56**, 13634–13643 (2022).
42. US Environmental Protection Agency. Hemispheric CMAQ model version 5.3beta output data—2016 seasonally averaged 108km for N. hemisphere, UNC Dataverse, V1. https://doi.org/10.15139/S3/QJDYWO (2019).
43. Crippa, M. *et al.* The HTAP_v3 emission mosaic: Merging regional and global monthly emissions (2000–2018) to support air quality modeling and policies. *Earth Syst. Sci. Data* **15**, 2667–2694. https://doi.org/10.5194/essd-15-2667-2023 (2023).
44. Zheng, B. *et al.* Changes in China's anthropogenic emissions and air quality during the COVID-19 pandemic in 2020. *Earth Syst. Sci. Data* **13**, 2895–2907. https://doi.org/10.5194/essd-13-2895-2021 (2021).
45. International Maritime Organization. Air pollution and energy efficiency: Study on the effects of the entry into force of the global 0.5% fuel oil sulphur content limit on human health. https://edocs.imo.org/FinalDocuments/English/MEPC70-INF.34€.docx (2016).
46. Guenther, A. B. *et al.* The model of emissions of gases and aerosols from Nature version 2.1 (MEGAN2.1) An extended and updated framework for modeling biogenic emissions. *Geosci. Model Dev.* **5**, 1471–1492 (2012).
47. van der Werf, G. R. *et al.* Global fire emissions estimates during 1997–2016. *Earth Syst. Sci. Data* **9**, 697–720 (2017).
48. Japan Meteorological Agency. Activity of each volcano. Webpage in Japanese. http://www.data.jma.go.jp/svd/vois/data/tokyo/volcano.html (2023).
49. Emery, C. *et al.* Recommendations on statistics and benchmarks to assess photochemical model performance. *J. Air Waste Manag. Assoc.* **67**, 582–598. https://doi.org/10.1080/10962247.2016.1265027 (2017).

Acknowledgements

Author contributions

S.I. conducted the analyses of measurements data, executed the model simulation, analysed the simulation results, and wrote the manuscript.

Competing interests

The author declares no competing interests.

Additional information

Supplementary Information The online version contains supplementary material available at https://doi.org/10.1038/s41598-023-43485-0.

Correspondence and requests for materials should be addressed to S.I.

Reprints and permissions information is available at www.nature.com/reprints.

Publisher's note Springer Nature remains neutral with regard to jurisdictional claims in published maps and institutional affiliations.